# Random scan optimization of a laser-plasma electron injector based on fast particle-in-cell simulations

P. Drobniak,[*] E. Baynard, C. Bruni, K. Cassou, C. Guyot, G. Kane, S. Kazamias,
V. Kubytskyi, N. Lericheux, B. Lucas, and M. Pittman
*Laboratoire de Physique des 2 Infinis Irène Joliot-Curie—IJCLab—UMR 9012*
*CNRS Université Paris Saclay, 91405 Orsay cedex, France*

F. Massimo
*Laboratoire de Physique des Gaz et des Plasmas—LPGP—UMR 8578,*
*CNRS, Université Paris-Saclay, 91405 Orsay, France*

A. Beck and A. Specka
*Laboratoire Leprince-Ringuet—LLR—UMR, 7638*
*CNRS Ecole polytechnique, 91128 Palaiseau cedex, France*

P. Nghiem and D. Minenna
*CEA-Irfu, Centre de Saclay, Université Paris-Saclay, 91191 Gif-sur-Yvette, France*

(Received 17 May 2023; accepted 15 August 2023; published 21 September 2023)

The optimization and advanced study of a laser-plasma electron injector are presented based on a truncated ionization injection scheme for high quality beam production. The SMILEI code is used with laser envelope approximation and a low number of particles per cell to reach computation time performances enabling the production of a large number of accelerator configurations. The developed and tested workflow is a possible approach for the production of a large dataset for laser-plasma accelerator optimization. A selection of functions of merit used to grade generated electron beams is discussed. Among the significant number of configurations, two specific working points are presented in detail. All data generated are left open to the scientific community for further study and optimization.

DOI: 10.1103/PhysRevAccelBeams.26.091302

## I. INTRODUCTION

While conventional particle accelerators are getting larger and larger for high energy physics (27.6 km for the LHC [1] and 97.8 km for the FCC project [2]), laser-driven wakefield acceleration (LWFA) is proven to be a promising technique for electron acceleration, yielding accelerating gradients 3 orders of magnitude greater than rf cavities, so in the range of 100 GV/m [3] thus requiring smaller facilities. Moreover, the mechanisms involved in the electron injection tend to produce very short bunches, in the range of a few fs duration [4]. These characteristics make laser-plasma acceleration an interesting candidate for a new range of applications, such as electron sources for very high energy electron radiation therapy [5] and x-ray free electron lasers (XFEL) [6].

Recent characteristics of electron bunches experimentally generated by LWFA lie in the range of a few hundreds of MeV [7,8] up to a few GeV [9], with pC [10] up to nC [11] charge, at a repetition rate of around 1 Hz [12]. They display a few percent energy spread [12], a normalized trace emittance around 1 mm mrad [8] and a divergence within the mrad range [8,13]. Note that these parameters are not at all achieved simultaneously.

Physical mechanisms driving the injection and acceleration processes in LWFA for laser-plasma injectors (LPI) are highly nonlinear and involve multiple coupled input parameters from the laser characteristics (focal spot position and size, focal distance, pulse duration and energy, polarization, wavelength, and spectrum) to plasma target parameters (gas choice, gas mixture composition, and density distribution). Theoretical results and experimental demonstration allow for the rough choice of plasma density profiles and laser parameters [14] in order to achieve the desired electron beam. Nevertheless, these scaling laws are usually not sufficient to precisely simulate the tuning and

---

[*] pierre.drobniak@ijclab.in2p3.fr

optimization of a laser-plasma accelerator (LPA). Moreover, due to high nonlinearity of the coupled processes and the experimental difficulty to accurately measure and store shot-to-shot fluctuations, the stability around optimal injection and acceleration configurations is a critical point.

Therefore, utilizing particle-in-cell (PIC) code, along with high performance computing resources and optimization algorithms, has proven to be a valuable tool in LPA design and active control studies. Bayesian optimization was already used and combined with experiments to deliver electron bunches at 1 Hz, with 250-MeV energy, subpercent energy spread, and spectral density of 4.7 pC/MeV [7]. To our knowledge, a massive generation of configurations (several thousands) in a short simulation time (a few hours), allowing the study of input-output correlations and with results open to the accelerator community has not been carried out yet.

The objective of this paper is to present the generation and analysis of a large amount of PIC simulation results in a short time (120 core. hour $\approx$30 min on 240 CPU cores), using high performance computing (HPC) resources with moderate total computational costs. The generated results are useful in multiple aspects. They will first allow for the discovery of specific working points, displaying interesting characteristics for the injector. These specific working points can later on be better assessed by finer PIC simulations and also investigated regarding their stability. Finally, all generated beams can serve as input for building surrogate models using machine learning techniques to predict beam parameters.

Section II starts with laser plasma injector parameters, introducing laser driver characteristics and plasma target configurations. Then the numerical setup for fast simulations recently allowed by the PIC code SMILEI [15] is presented and the massive random scan settings are introduced.

Section III gives an overview of the generated dataset where correlations between plasma target input parameters and electron beam output parameters are highlighted. Several possible functions of merit to quickly grade and compare the generated beams are discussed. Finally, two different types of LPI configurations generating specific electron beams are extracted and further discussed.

The results presented in this article are part of the PALLAS [16] project at IJCLab, which uses the 1.6-J moderate energy and 10-Hz repetition rate laser provided by the LaseriX platform [17]. PALLAS aims at optimizing an LPI for the EUPRAXIA project [18], producing electron beams within the 150–250 MeV energy range, less than 5% energy spread, more than 30 pC charge, and a normalized emittance of less than 2 μm.[1]

In the following, will be referred as "*filter*", the condition "$Q > 30$ pC & $E_{\mathrm{med}} > 150$ MeV & $\delta E_{\mathrm{mad}} < 5\%$ & $\epsilon_{y,n} < 2$ μm", where $Q$ is the charge, $E_{\mathrm{med}}$ the median energy, $\delta E_{\mathrm{mad}} = \sigma_{\mathrm{mad}}/E_{\mathrm{med}}$ (with $\sigma_{\mathrm{mad}}$ the median absolute deviation) and $\epsilon_{y,n}$ the normalized emittance in $y$ direction (laser polarization direction) defined as $\epsilon_{y,n} = \frac{1}{m_0 c}\sqrt{\langle y^2\rangle\langle p_y^2\rangle - \langle y p_y\rangle^2}$ [19] (with $m_0$ the electron mass, $c$ the speed of light in vacuum, and $p_y$ the momentum in $y$ direction). The choice of median values over mean values is made as investigated and explained in [20]. In case of plasma generated electron beams, it is more statistically robust than conventional rms (root mean square). For a Gaussian distribution, it is, however, possible to retrieve the rms value $\sigma_{\mathrm{rms}}$ using the relation $\sigma_{\mathrm{rms}} \simeq 1.4826\sigma_{\mathrm{mad}}$.

## II. PARTICLE-IN-CELL SCAN SETTINGS

### A. LPI parameters

Experimental laser driver characteristics provided by LaseriX are linearly polarized fifth order flattened Gaussian beam (FGB) [21] with 810-nm central wavelength, spectral width of $\Delta\lambda = 30$ nm, a maximum energy on target of $1.6 \pm 0.1$ J, $35 \pm 5$ fs duration ($10.5 \pm 1.5$ μm length) at 10 Hz. This corresponds to a peak power of 40 TW. The laser-driver beam is focused with a 1.5-m focal length off-axis parabola to a waist of $w_0 = 19$ μm. This leads to a laser intensity $a_0$ reaching its maximum in vacuum $a_{0,\mathrm{vac,max}} = 1.40$ ($4 \times 10^{18}$ W cm$^{-2}$). A laser upgrade could lower the pulse duration to 30 fs and increase the energy to 2.4 J, yielding an intensity of $a_{0,\mathrm{vac,max}} = 1.85$. The Rayleigh length is $x_R = 1.42$ mm.

For the present electron density (see the end of II A), the laser intensity is too low for self-injection (similar range studied in [22]). So a nitrogen ionization injection scheme [23] is chosen, using helium as the main gas, in a $\mathrm{He} + \mathrm{N}_2$ mixture.

The plasma self-focusing in the target allows for an increase in $a_0$, high enough to ionize the inner shell electrons of nitrogen and potentially inject them in the wake. Indeed, the barrier suppression ionization (BSI) potentials of $\mathrm{N}_2$ two last electrons at 800 nm [14] are $a_{0,\mathrm{BSI,N^{5+}\to N^{6+}}} = 2.21$ and $a_{0,\mathrm{BSI,N^{6+}\to N^{7+}}} = 2.77$.

As suggested in [10,23,24] and further investigated in [25,26], the plasma target is split into two stages (Fig. 1). A first stage (chamber 1) with helium mixed with nitrogen (at molar concentration $c_{\mathrm{N}_2}$ within a few percent range) dedicated to laser self-focusing and injection followed by a second stage (chamber 2) with helium only allowing for truncation of injection (no dopant anymore) and acceleration of the injected electron bunch. Since the two chambers share a common aperture (laser travels from chamber 1 to chamber 2), each chamber is set to the same pressure $p$ in order to prevent various species convection from one chamber to the other. The pressure $p$ then

---

[1] The beam divergence optimization is out of the scope of the present study.

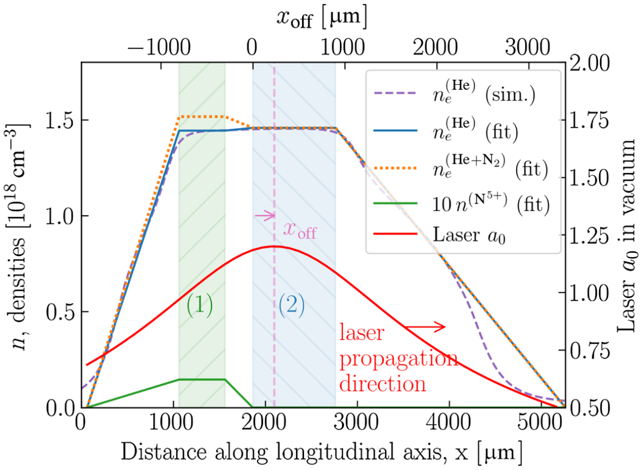

FIG. 1. Example of electron density and dopant ion density for a target with $p = 30$ mbar and $c_{N_2} = 1\%$. First and second plateaus, respectively, correspond to chamber 1 and chamber 2 and are delimited with dashed areas, respectively, green and blue. $n_e^{(\text{He})}$ (sim.) is the helium electron density, as simulated by OpenFOAM and assuming full ionization and $n_e^{(\text{He})}$ (fit) is the corresponding polygonal fit. $n_e^{(\text{He+N}_2)}$ (fit) is the electron density fit on the mixture He + N$_2$, assuming full ionization of He and ionization of N$_2$ up to the fifth level. The atomic density of N$^{5+}$ ions is $n^{(\text{N}^{5+})}$. The envelope of a laser pulse traveling from left to right with maximum intensity in vacuum $a_{0,\text{vac,max}} = 1.2$ and focal position in vacuum $x_{\text{off}} = 235$ μm is added ($x_{\text{off}}$ reference starts at chamber 2 beginning).

describes both the He + N$_2$ mixture pressure in chamber 1 and the helium pressure in chamber 2. For a given pressure, the ratio between the electron densities of chamber 1 and 2 thus only comes from additional dopant concentration. The profile used here is generated by OpenFOAM [27] and a polygonal fit allows for a simplified direct variation of dopant concentration and overall pressure in the PIC simulations.

The first constraint on the choice of pressure is self-focusing. Based on the available laser power $P$, the corresponding electron density required for self-focusing [14] is given by $P > P_c$ with $P_c[GW] \simeq 17(\lambda_p/\lambda)^2$ where $P_c$ is the critical laser power required to trigger the effect, $\lambda_p$ and $\lambda$, respectively, the plasma and laser wavelengths. Here the electron density necessary for self-focusing is $n_{e,sf} \approx 6.3 \times 10^{17}$ cm$^{-3}$. The pressure thus has to be greater than the self-focusing pressure $p > p_{\text{He,sf}} \approx 13$ mbar (assuming full ionization of helium).

A second constraint on pressure is the optimal energy conversion between the laser driver and the plasma wave (resonant density). Based on the work done by Faure [4] and assuming a linear regime, one has to ensure $k_p L_0 = \sqrt{2}$, with $k_p$ the plasma wave number and $L_0$ the FWHM laser pulse length. In the present case, this yields a resonant electron density of $n_{e,\text{res}} \approx 5.1 \times 10^{17}$ cm$^{-3}$ with corresponding fully ionized helium resonant pressure $p_{\text{He,res}} \approx 10$ mbar. Thus, a helium pressure starting at $p_{\text{He,res}}$ up to a value of 100 mbar (experimental limit) is chosen, so a range of [10, 100] mbar.

With the choice of laser waist $w_0 = 19$ μm within the pressure range mentioned above, the focal spot is roughly matched for a potential bubble regime. Indeed, one can use the formula given by [14]: $w_0 \simeq R_b = 2c\sqrt{a_0}/\omega_p$ where $R_b$ is the bubble radius and $\omega_p$ the plasma frequency. Using the extreme possible values for pressure and laser $a_0$, the corresponding matched spot size range is [4.5, 20.5] μm, so in agreement with the laser waist $w_0 = 19$ μm in vacuum (actually reaching even lower values due to self-focusing).

The depletion length $L_{pd}$ and dephasing length $L_{d,\text{bubble}}$ (if matched spot size) are defined as [14] $L_{pd} \simeq (\omega_0/\omega_p)^2 c\tau$ and $L_{d,\text{bubble}} \simeq (2/3)(\omega_0/\omega_p)^2 w_0$ with $\omega_0$ the laser frequency, $\omega_p$ the plasma frequency, and $\tau$ the laser duration. This yields for $n_e = 5 \times 10^{18}$ cm$^{-3}$ (dimensioning case), $L_{pd} \simeq 3.65$ mm, and $L_{d,\text{bubble}} \simeq 4.41$ mm, well above the Rayleigh length $x_R$. Therefore $x_R$ is used for dimensioning the accelerating stage of our plasma target (chamber 2), so approximately 1 mm.

The current experimental design for PALLAS project allows to vary four input parameters: (i) pressure $p \in [10; 100]$ mbar; (ii) laser $a_{0,\text{vac,max}} \in [1.1; 1.85]$ (upper boundary to account for later laser upgrade); (iii) dopant concentration $c_{\text{N}_2} \in [0.2; 12]\%$, defined as the partial pressure ratio of dopant to mixture pressure (0.2% is the minimum that can be experimentally achieved here, the upper value is based on previous work [7]); (iv) focal position offset $x_{\text{off}} \in [-400; 1800]$ μm, with origin $x_{\text{off}} = 0$ defined as the focus position in vacuum and provided on the upper horizontal axis of Fig. 1 (inspired by [7,8,14]).

### B. Particle-in-cell simulations setup

Simulations of electron injection and acceleration in the plasma have been performed with the open source particle-in-cell (PIC) code SMILEI [15,28].

The physical setup assumes a laser propagation in $x$ direction and transverse plane on $y$ and $z$ axis. In case of cylindrical coordinates, space variables are $(r, \theta, x)$, with $x$ the laser propagation direction.

To speed up LWFA simulations, which typically have a considerable computational cost, an envelope model [29,30] was used in cylindrical geometry, with only one azimuthal mode. Indeed, the coupling of cylindrical symmetry and envelope approximation can greatly reduce PIC simulations computational costs for LWFA, as shown in [30–32]. The theoretical formula for FGB propagation was implemented (based on theory [33] and FBPIC implementation [34]) and the laser was modeled as a fifth-order FGB, with a waist of $w_0 = 19$ μm, 35-fs FWHM unchirped Gaussian temporal profile and $a_{0,\text{vac,max}}$ in [1.10,1.85]. Each simulation ran on five compute nodes with a total of

TABLE I. Input parameters investigated for RS1, RS2, RS3, RS4, and RS5. $\mathrm{SND}_{900}$ and $\mathrm{SND}_{1200}$ are skew normal distributions [37], respectively, centered on 900 and 1200 μm. Other parameters are picked randomly within the specified range.

| | RS1 | RS2 | RS3 | RS4 | RS5 |
|---|---|---|---|---|---|
| $p$ [mbar] | [10;100] | [10;90] | [10;60] | [30;100] | [10;100] |
| $a_{0,\mathrm{vac,max}}$ | [1.1;1.45] | [1.1;1.45] | [1.4;1.85] | [1.1;1.45] | [1.1;1.45] |
| $x_{\mathrm{off}}$ [μm] | $\mathrm{SND}_{900}$ | $\mathrm{SND}_{1200}$ | [800;1800] | [800;1800] | [−400; 600] |
| $c_{\mathrm{N}_2}$ [%] | [0.2;12] | [0.5;2] | [0.5;12] | [0.5;2] | [0.5;2] |

240 CPU-core (10 MPI processes each using 24 OpenMP threads).

Helium macroparticles were initialized and fully ionized, while nitrogen macroparticles were initialized and ionized up to the five first levels, both with initial temperature equal to zero (cold plasma). This approximation is justified by the fact that all helium electrons and the five first electrons of nitrogen are already ionized 50 fs ahead of the pulse center, so approximately $1.5 \times T_{\mathrm{laser,FWHM}}$, with $T_{\mathrm{laser,FWHM}}$ the FWHM laser pulse duration. The main part of the pulse will thus propagate in an already ionized plasma of $\mathrm{He}^{2+}$ and $\mathrm{N}^{5+}$.

A moving window is used to follow the laser pulse in its propagation and keep only the physics of interest inside the simulation domain. Its characteristics are defined in 2D, with size in the $(x,\ r)$ space set to $64\ \mu\mathrm{m} \times 143\ \mu\mathrm{m}$ $(6.10L_0 \times 7.53w_0)$, and a resolution of $\Delta x = 0.1\ \mu\mathrm{m}$ and $\Delta r = 0.16\ \mu\mathrm{m}$ with an integration time step of $\Delta t = 0.8\Delta x/c = 0.27$ fs. The laser pulse center is in the simulation window, located $1.25 \times T_{\mathrm{laser,FWHM}}$ from the window front edge, since $\mathrm{He}^{2+}$ and $\mathrm{N}^{5+}$ are already ionized at $1.5 \times T_{\mathrm{laser,FWHM}}$.

For the simulation diagnostics, the electrons from He, the electrons from the five first levels of $\mathrm{N}_2$, and $\mathrm{N}_2$ inner shell electrons "born" from tunnel ionization were tracked separately. This choice allowed us to check which electrons came from ionization injection and which from other injection mechanisms, e.g., downramp injection [35].

The electron density profile is read as input by the solver, as described in Fig. 1, where a polygonal fit on the OpenFOAM-simulated electron profile was performed, with space dimensions kept constant and where only the values of electron densities in plateau 1 and 2 were varied (through $p$ and $c_{\mathrm{N}_2}$). For each species, only one macroparticle per cell (ppc) is used. The validity of such an approximation was checked by running a low and a high charge case, respectively, injecting 30 and 160 pC and comparing them with 8 ppc cases. The relative maximum error was 1% on $E_{\mathrm{med}}$, 10% on $\delta E_{\mathrm{mad}}$, 10% on $Q$, and 8% on $\epsilon_{y,n}$, which is acceptable for typical experimental measurement precision on these parameters.

The gain in computation time given by the reduction of 8 to 1 ppc is significant. For the low charge case, the computation time went from 450 core. hour (8 ppc case) to 130 core. hour to (1 ppc case), so a speedup of 3.5. For the high charge case, simulations were 4 times faster from 700 core. hour to 170 core. hour for 8 ppc and 1 ppc cases, respectively. So each scan simulation is performed with 1 ppc and the average simulation time is approximately 30 min on 240 CPU cores (time depends on the injected charge and the resulting number of macroparticles to track). Each configuration directory weighs around 5 GB.

### C. Scan settings

Using the GENCI high performance computing facility Irene-Joliot Curie [36], five massive random scans (RS) called RS1, RS2, RS3, RS4, and RS5 in the $(p,\ a_{0,\mathrm{vac,max}},\ x_{\mathrm{off}},\ c_{\mathrm{N}_2})$-space were performed, with 2401 configurations each, so a total of 12 005 simulations. Each RS ran for approximately 4 h (limited due to the maximum number of jobs authorized in the queue) and generated around 10 TB of data. The input parameter space explored is presented in Table I, where $\mathrm{SND}_{900}$ and $\mathrm{SND}_{1200}$ are skew normal distributions [37], respectively, centered on 900 and 1200 μm and all other parameters ranges follow random distributions.

Random scans make easier the visualization of the 4D-input space on 2D or 3D meshes since points do not overlap. They also allow for randomly distributed small variations of input parameters on which the output might be very sensitive. Nondeterministic randomized combinations of the hyperparameter input space have been generated (see git repository for more information [38]).

## III. RESULTS

### A. Postprocessing

A Python script based on HAPPI library [39] is used for postprocessing to extract the electron beam and laser parameters [38]. For the injection, the inner shell electrons from $\mathrm{N}^{5+}$ were tracked. The electron beam data are extracted at the last simulation time step (end of the plasma density out ramp) and a lower cutoff energy of 25 MeV is applied on the electron bunch energy distribution. Low charge beams below 0.3 pC are not considered. Electrons originating from helium are not included in the resulting

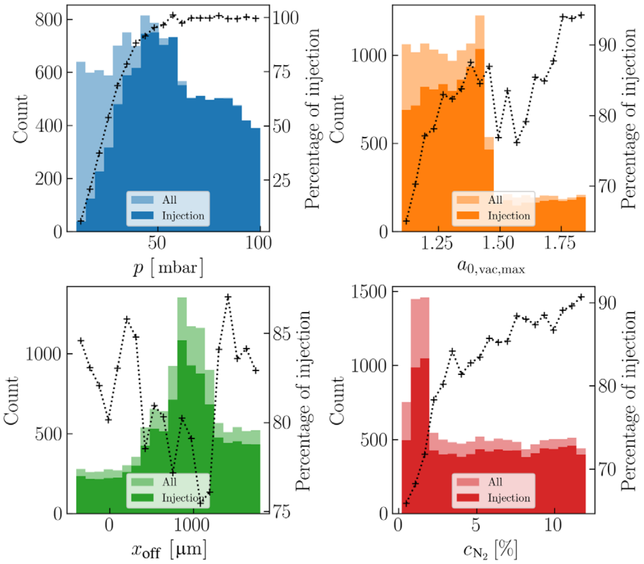

FIG. 2. Histogram comparison between injection and noninjection for all RS (bins = 20). All configurations are displayed in light colors, the ones leading to injection are in dark colours. For each bin, the percentage of injection is represented by black crosses.

beam since they are very rarely trapped by self-injection ($a_0 > 4$) and do not contribute to the overall charge.

All postprocessing scripts are available online [38].

### B. Injection conditions

The scans RS1, RS2, RS3, RS4, and RS5 show effective injection (i.e., the integrated charge above 25 MeV must be superior to 3 pC), respectively, in 80%, 66%, 83%, 92% and 82% of cases, so a total of 10 025 generated beams. RS2 tried very downstream focuses so injected less than other RS. RS4 did not try very low pressures, so ensured very often self-focusing. The maximum effective $a_{0,\mathrm{eff,max}}$ reached within propagation was high enough for ionizing $N_2$ inner shell electrons and for generating a large bubble, thus favoring ionization injection. The injection triggering trend for each input parameters is summarized in Fig. 2, where all configurations tried in the ($p$, $a_{0,\mathrm{vac,max}}$, $x_\mathrm{off}$, $c_{\mathrm{N}_2}$)-space are displayed in light colors while the ones leading to injections are in dark ones.

Injection triggering is favored by high $p$ (stronger self-focus), high $a_{0,\mathrm{vac,max}}$ (higher tunnel ionization rate), and high $c_{\mathrm{N}_2}$ ($\mathrm{N}_2$ participates in the background electron density). An upstream $x_\mathrm{off}$ means high intensity while entering chamber 1 so strong self-focusing and thus high tunnel ionization rate in the dopped region. A downstream $x_\mathrm{off}$ has lower intensity while entering chamber 1 and a maximum reached later in the propagation. If this maximum happens at the very end of chamber 1, injection in this

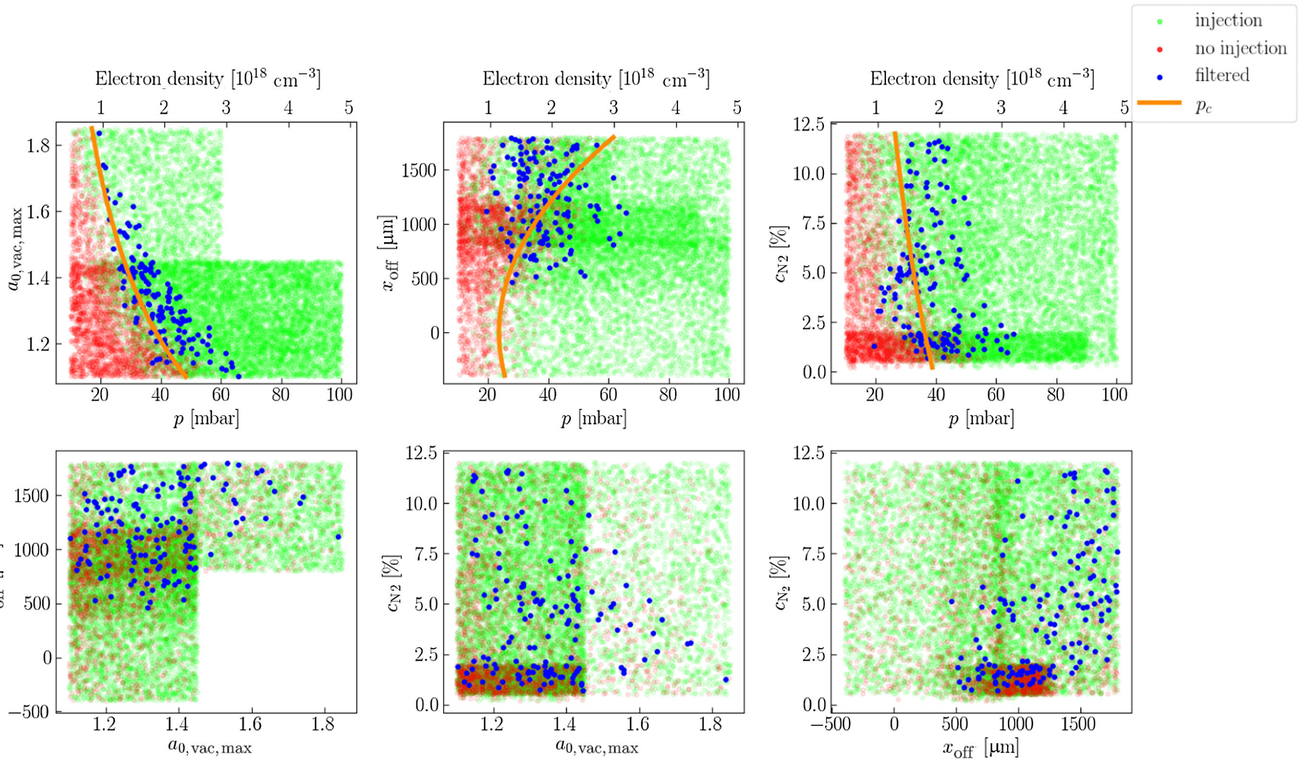

FIG. 3. Comparison between injection (green dots) and noninjection (red dots) for all configurations in the input space. Critical pressure (or electron density) required for self-focusing is computed using the formula for self-focusing given in [40], where hidden parameters $x_\mathrm{off}$ and $c_{\mathrm{N}_2}$ in the $(p, a_0)$-graph, $a_0$ and $c_{\mathrm{N}_2}$ in the $(p, x_\mathrm{off})$-graph, and $a_0$ and $x_\mathrm{off}$ in the $(c_{\mathrm{N}_2})$-graph were averaged. Configurations satisfying the filter defined in Sec. I are displayed with blue dots.

case is low. The unexpected rise for $x_{\mathrm{off}}$ above 1000 μm is explained by the hidden $a_{0,\mathrm{vac,max}}$ parameter, which is higher in the case of RS3.

Cross correlations on input parameters triggering injection are presented in Fig. 3, where configurations producing the target electron beam (satisfying the filter defined in Sec. I) were identified in dark blue.

Using the formula for self-focusing given in [40], the "mean" critical pressure $p_c$ required for the laser self-focusing in the plasma target first chamber is added through the yellow curve. The term mean refers to an average on the two hidden parameters of each 2D plot.

In the $(p, a_{0,\mathrm{vac,max}})$-graph of Fig. 3, one can see a correlation for injection between $p$ and $a_{0,\mathrm{vac,max}}$ and a diffuse transition between the "no-injection" area to the "injection" area, well fitted by the $p_c$ curve. As a matter of fact, injection needs self-focusing to appear and since there are two hidden parameters, this transition is diffuse. The target beams lie at the transition to injection because too much self-focusing will induce injection in a large volume (longitudinally and transversally) and thus produce too much charge leading to a beam with too high energy spread, emittance and possibly too low energy (beam-loading). One can also note that the filtered beams can be produced within all the tested $a_{0,\mathrm{vac,max}}$ range, while $p$ has to be kept within [20; 70] mbar.

In the $(p, x_{\mathrm{off}})$ view, a correlation for triggering of injection also appears between $p$ and $x_{\mathrm{off}}$, fitted by $p_c$, since an upstream focus means that the laser enters chamber 1 with a higher $a_0$, thus facilitating self-focusing. For very high $x_{\mathrm{off}}$, two separate injection regions appear and there is no sharp transition by varying $p$. This is explained in the $(a_{0,\mathrm{vac,max}}, x_{\mathrm{off}})$ graph, where one sees that very high $a_{0,\mathrm{vac,max}}$ were also tried for downstream focuses (contribution from RS3). Here again, the target beams lie at this diffuse transition since they require a small injection volume. There is a preferred region in $x_{\mathrm{off}}$ to produce them above 500 μm since the upstream focus will inject too much charge: space charge and beam loading effects will affect the energy, energy spread, and emittance. Higher $x_{\mathrm{off}}$ above 1800 μm are also interesting to generate the target beams but seem to require always higher $a_{0,\mathrm{vac,max}}$ which are out of the present study.

In the $(p, c_{N_2})$ graph, one sees a threshold on pressure $p$ (required for self-focusing to happen) correlated with the dopant concentration $c_{N_2}$. The transition between no-injection and injection is well described by $p_c$.

It is hard to identify particular trends in the $(a_{0,\mathrm{vac,max}}, x_{\mathrm{off}})$, $(a_{0,\mathrm{vac,max}}, c_{N_2})$, or $(x_{\mathrm{off}}, c_{N_2})$ views, both for the injection points and for the target beams since the pressure $p$ plays a very significant role but is a hidden parameter in these three graphs. Still, one sees that focusing too upstream will not produce target beams. The reason for this lies in a strong self-focusing producing very high-charge beams displaying poor characteristics.

As a conclusion on the injection tendencies, a strong dependance on $p$ appears to trigger injection with a diffuse transition from no injection to injection in the $(p, a_{0,\mathrm{vac,max}})$, $(p,\ x_{\mathrm{off}})$ and $(p,\ c_{N_2})$ graphs since injection requires self-focusing to appear and this phenomenon is dependent on the electronic density (mostly $p$ but also $c_{N_2}$ through outer shell electrons) and the laser intensity at chamber 1 entrance, so $a_{0,\mathrm{vac,max}}$ and $x_{\mathrm{off}}$. This transition is well fitted by the theoretical curve $p_c$ for self-focusing. A control on the volume of injection is a critical point for the target beams.

### C. Electron beams evaluation

The output space of interest for the present study is defined by the following electron beam parameters: $(Q, E_{\mathrm{med}}, \delta E_{\mathrm{mad}}, \epsilon_{y,n})$. Divergence was not included since this parameter can be controlled by optimizing the plasma outramp. It was already studied in [19,41] and experimentally demonstrated [42]. All results are available online and the reader can use the online dashboard for their own data exploration [38].

In addition to the filter condition ($F = 1$ if the filter is fulfilled, 0 otherwise), different functions of merits inspired by the literature are tried[2] (Eq. (1):

$$\begin{aligned} f_1 &= \frac{E_{\mathrm{med}}^2 \cdot Q}{\sigma_{\mathrm{mad}} \epsilon_{y,n}}, \\ f_2 &= \frac{E_{\mathrm{med}} \cdot \sqrt{Q}}{\sigma_{\mathrm{mad}}}, \\ f_3 &= \frac{E_{\mathrm{med}} \cdot Q}{\sigma_{\mathrm{mad}}}, \\ f_4 &= \frac{E_{\mathrm{med}} \cdot Q}{\sigma_{\mathrm{mad}} \sqrt{\epsilon_{y,n} \epsilon_{z,n}}}. \end{aligned} \tag{1}$$

There is no universal function of merit since each application requires the optimization of given sets of beam characteristics: $f_1$ gives more importance to $E_{\mathrm{med}}$, $f_2$ is the function used by Jalas *et al.* in their Bayesian optimization [7], $f_3$ insists more on charge, $f_4$ includes the normalized transverse emittances $\epsilon_{y,n}$ (laser polarization direction) and $\epsilon_{z,n}$ to optimize the brightness.

### D. Best beams generated

Beams were selected to a cutoff of 90% of each function maximum. Results are presented in Fig. 4, where three views of the output space were chosen: $(Q, E_{\mathrm{med}})$, $(Q, \delta E_{\mathrm{mad}})$, and $(Q, \epsilon_{y,n})$. From now on, the terms $S1$,

---

[2] "Functions of merit" should not be mistaken with "objective functions" since the former allow for a scalar view of the output space, while the latter are used in a decision process (in a Bayesian optimization process, for example).

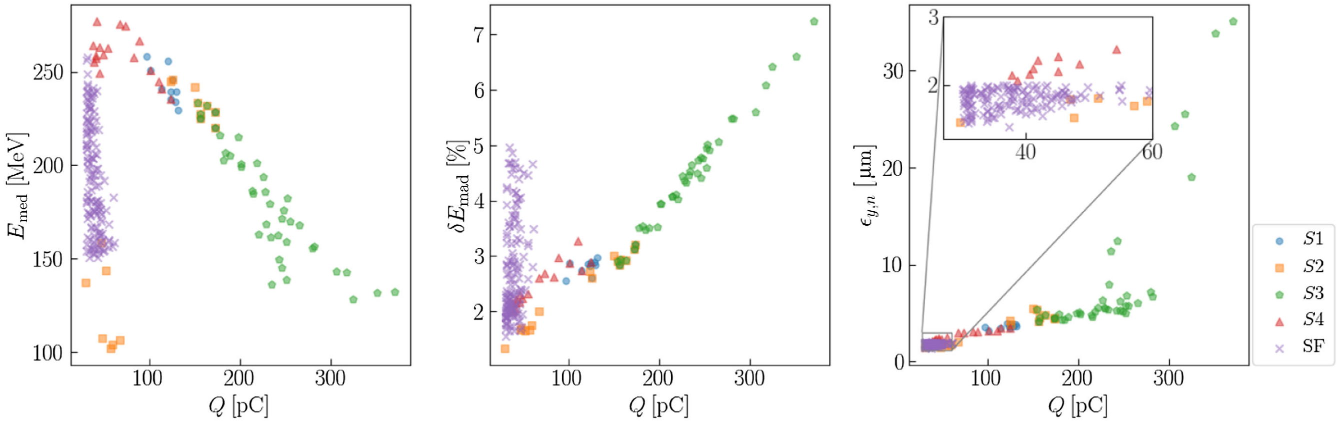

FIG. 4. Three views of simulations results in the output space as function of the injected charge $Q$. Beams selected by the functions of merit with a cutoff at 90% of $f_1, f_2, f_3, f_4$ maximum and beams in the filter defined in Sec. I are compiled in sets, respectively, denoted as $S1$, $S2$, $S3$, $S4$, and $SF$.

$S2$, $S3$, $S4$, and $SF$ are used to write about sets, respectively, selected by $f_1$, $f_2$, $f_3$, $f_4$, and $F$.

In the $(Q, E_{\text{med}})$ view, a maximum appears for $E_{\text{med}}$ for $Q$ within [80, 100] pC, followed by a linear decrease with $Q$. Such a behavior is explained by beam-loading effects, where more charge flattens the longitudinal accelerating field.

The $(Q, \delta E_{\text{mad}})$ graph shows a quasilinear increase of $\delta E_{\text{mad}}$ with $Q$, except for a specific region within [80, 150] pC, where a stagnation appears (optimal working point).

The $(\epsilon_{y,n}, Q)$ graph also displays a linear increase of $\epsilon_{y,n}$ with $Q$, the slope being more pronounced for $S3$ which favors high charges. High charge leads to strong space-charge effects and a higher normalized transverse emittance. Furthermore, high charge beams are loaded even far from axis, inducing strong oscillations of the electrons in the transverse plane and thus high $\epsilon_{y,n}$.

Looking at functions of merit, one can say that $f_1$ and $f_4$ are good compromises in terms of $Q$, $\delta E_{\text{mad}}$, $E_{\text{med}}$, and $\epsilon_{y,n}$, the latter remains a bit too high for the beams to be in $SF$. $f_2$ favors two areas of the output space, so its use in a decision process might not be optimal for the present parameter range. $f_3$ is useful for highlighting very high charge beams, regardless of their $\epsilon_{y,n}$.

The results generated by all RS produced 145 configurations in $SF$. $f_1$, $f_2$, and $f_4$ managed to approach it, with only one configuration in $S2 \cup SF$. In this selection, the maximum $E_{\text{med}}$ was 257 MeV and the lowest $\delta E_{\text{mad}}$ reached 1.54% ($\sigma_{\text{mad}} = 3.27$ MeV). The charge is very limited, since $Q$ above 61 pC generated $\epsilon_{y,n}$ above the filter limit.

### E. Best injector configurations

The input space parameters of $S1$, $S2$, $S3$, $S4$, and $SF$ are presented in Fig. 5. An axis with the variable $a_{0,\text{eff,max}}$ is

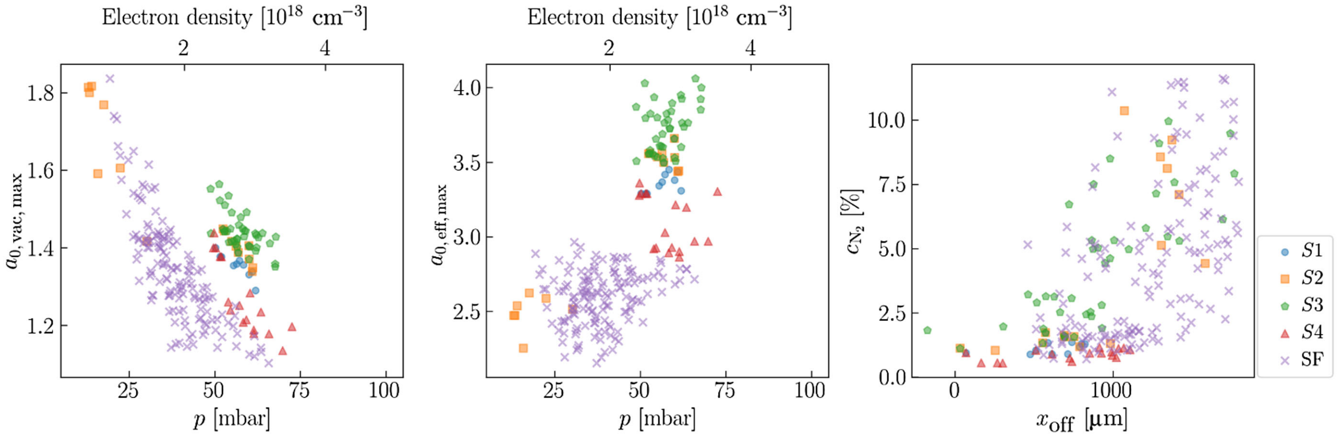

FIG. 5. Three views of simulations results in the $(p, a_{0,\text{vac,max}}, x_{\text{off}}, c_{\text{N}_2})$ input space, where a plot with $a_{0,\text{eff,max}}$ was added, corresponding to the effective maximum laser intensity reached by the laser in the plasma. Beams selected by the functions of merit with a cutoff at 90% of $f_1, f_2, f_3, f_4$ maximum and beams in the filter defined in Sec. I are compiled in sets, respectively, denoted $S1$, $S2$, $S3$, $S4$, and $SF$.

added, which corresponds to the maximum of $a_0$ effectively reached by the laser during its propagation in the plasma.

As a first consideration on configuration distribution in Fig. 5, one can see that $S1$, $S2$, $S3$, $S4$, and $SF$ all seem to gather in different areas of the $(p, a_{0,\mathrm{vac,max}})$ and $(p, a_{0,\mathrm{eff,max}})$-spaces, with a slight overlap between $S2$ and $S3$, as already seen in Fig. 4. In the $(x_{\mathrm{off}}, c_{\mathrm{N_2}})$-space, $S2$, $S3$, and $SF$ occupy large areas, which means that $x_{\mathrm{off}}$ or $c_{\mathrm{N_2}}$ were not the critical variables for each set. However, $S1$ and $S4$ occupy well-defined areas, with low $c_{\mathrm{N_2}}$, where $S1$ is precisely located around $x_{\mathrm{off}} = 700$ μm and $S4$ is more flexible on $x_{\mathrm{off}}$.

High charge beams ($S3$) originated from the highest $p \times a_{0,\mathrm{vac,max}}$ combination, resulting in the highest $a_{0,\mathrm{eff,max}}$, above 3.5. They were produced within a wide range of $x_{\mathrm{off}}$ and $c_{\mathrm{N_2}}$.

On the contrary, low charge beams (from $SF$ for instance) originated from relatively low $p$ and $a_{0,\mathrm{vac,max}}$, inducing an $a_{0,\mathrm{eff,max}}$ in the range of $\mathrm{N}^{5+}$ and $\mathrm{N}^{6+}$ BSI.

The optimal zone with highest $E_{\mathrm{med}}$ in Fig. 4 $(Q, E_{\mathrm{med}})$-space is described by $S4$ and corresponds to $p \in [50; 70]$ mbar, $a_{0,\mathrm{vac,max}} \in [1.1; 1.4]$ and $x_{\mathrm{off}} \in [0; 1100]$ μm leading to an $a_{0,\mathrm{eff,max}} \in [2.9; 3.3]$.

The stagnation area identified in Fig. 4 $(Q, \delta E_{\mathrm{mad}})$-space described by $S1$ is reached for $p \approx 60$ mbar, $a_{0,\mathrm{vac,max}} \approx 1.4$ and $x_{\mathrm{off}} \in [500; 700]$ μm, leading to an $a_{0,\mathrm{eff,max}} \approx 3.5$. These beams were obtained with very low $c_{\mathrm{N_2}}$, below 2%.

Beams in $SF$ originate from a wide range of $p$ and $a_{0,\mathrm{vac,max}}$ but in a certain $p \times a_{0,\mathrm{vac,max}}$ area. The focus $x_{\mathrm{off}}$ had to be downstream 500 μm. No particular constraint appears on $c_{\mathrm{N_2}}$. By looking at the $(p, a_{0,\mathrm{eff,max}})$-space, one sees that $a_{0,\mathrm{eff,max}}$ has to remain within the range of $\mathrm{N}^{5+}$ and $\mathrm{N}^{6+}$ BSI intensities to trigger tunnel ionization but not too strongly. This reduces the volume of injection either longitudinally (reduced injection length) or transversally (no injection far from axis).

### F. Selected configurations

In this section, we analyze two LPI configurations originating from very different combinations of input parameters: (i) best of $f_3$ (configuration 3702, comes from RS2); and (ii) $\delta E_{\mathrm{mad}}^{(\mathrm{min})}$ (lowest energy spread) in the filter (configuration 7516, comes from RS4).

The spectra of those two beams are presented in Fig. 6.

The input and output parameters of these two configurations are presented in Table II.

Configuration 3702 corresponds to relatively high pressure ($p = 58.6$ mbar) and relatively strong intensity ($a_{0,\mathrm{vac,max}} = 1.43$) at upstream focus ($x_{\mathrm{off}} = 558$ μm) leading to strong self-focusing ($a_{0,\mathrm{eff,max}} = 3.73$), so inducing a very high injected charge ($Q = 198$ pC) even for a low dopant concentration ($c_{\mathrm{N_2}} = 1.88\%$). This high charge induces a high emittance ($\epsilon_{y,n} = 5.03$ μm) and does not fit $SF$. Configuration 7516 was generated with moderate pressure ($p = 47.8$ mbar), relatively low intensity ($a_{0,\mathrm{vac,max}} = 1.23$), a downstream focus ($x_{\mathrm{off}} = 1680$ μm) leading to mild self-focusing ($a_{0,\mathrm{eff,max}} = 2.58$) in a medium dopant concentration ($c_{\mathrm{N_2}} = 6.17\%$), so a quite low injected charge ($Q = 30$ pC). This beam displays very small energy spread ($E_{\mathrm{mad}} = 1.55\%$) and emittance ($\epsilon_{y,n} = 1.74$ μm) while remaining in $SF$.

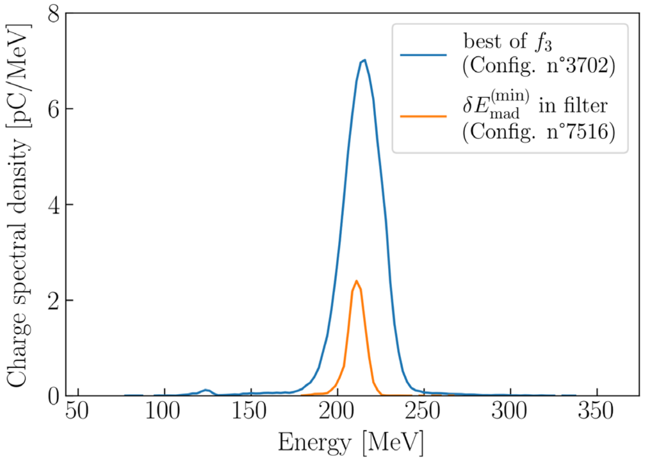

FIG. 6. Spectra of the beams generated by the two simulations of configurations 3702 and 7516, respectively, corresponding to the best of $f_3$ and $E_{\mathrm{mad}}^{(\mathrm{min})}$ (lowest energy spread) in the filter from Sec. I. Electrons below 25 MeV were not captured.

Beam 3702 is interesting for high energy physics and radiation therapy application, while beam 7516 could be an interesting candidate for X-FEL generation due to its reduced energy spread.

More details on the beam dynamics of configurations 3702 and 7516 are given in Figs. 7 and 8, where self-focusing occurs for configuration 3702. $a_0$ reaches its maximum upstream chamber 2 entrance, followed by laser

TABLE II. Input and beam parameters of LPI configurations 3702 and 7516.

| | Best of $f_3$ | $\delta E_{\mathrm{mad}}^{(\mathrm{min})}$ in filter |
|---|---|---|
| N° | 3702 | 7516 |
| Origin | RS2 | RS4 |
| $p$ (mbar) | 58.6 | 47.8 |
| $a_{0,\mathrm{vac,max}}$ | 1.43 | 1.23 |
| $x_{\mathrm{off}}$ (μm) | 558 | 1680 |
| $c_{\mathrm{N_2}}$ (%) | 1.88 | 6.17 |
| $a_{0,\mathrm{eff,max}}$ | 3.73 | 2.58 |
| $Q$ (pC) | 198 | 30 |
| $E_{\mathrm{med}}$ (MeV) | 215 | 212 |
| $\delta E_{\mathrm{mad}}$ (%) | 3.53 | 1.55 |
| $\epsilon_{y,n}$ (μm) | 5.03 | 1.74 |

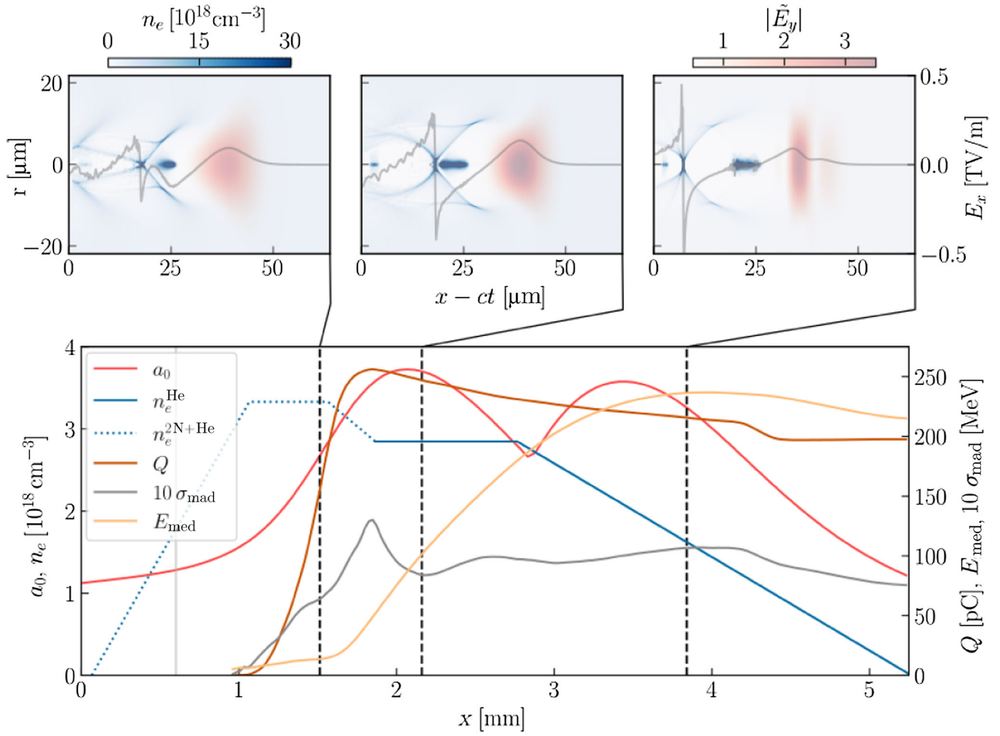

FIG. 7. Evolution of laser ($a_0$) and beam parameters ($Q$, $E_{\mathrm{med}}$, $\sigma_{\mathrm{mad}}$) during propagation for configuration 3702. The electron density profile for chamber 1 (dashed line) and chamber 2 (solid line) is added. Laser travels from left to right. Three snapshots display the injection process at three different timesteps (increase of $a_0$, maximum of $a_0$, and beam at plasma outramp). Entrance of chamber 1 is located at $x = 1$ mm.

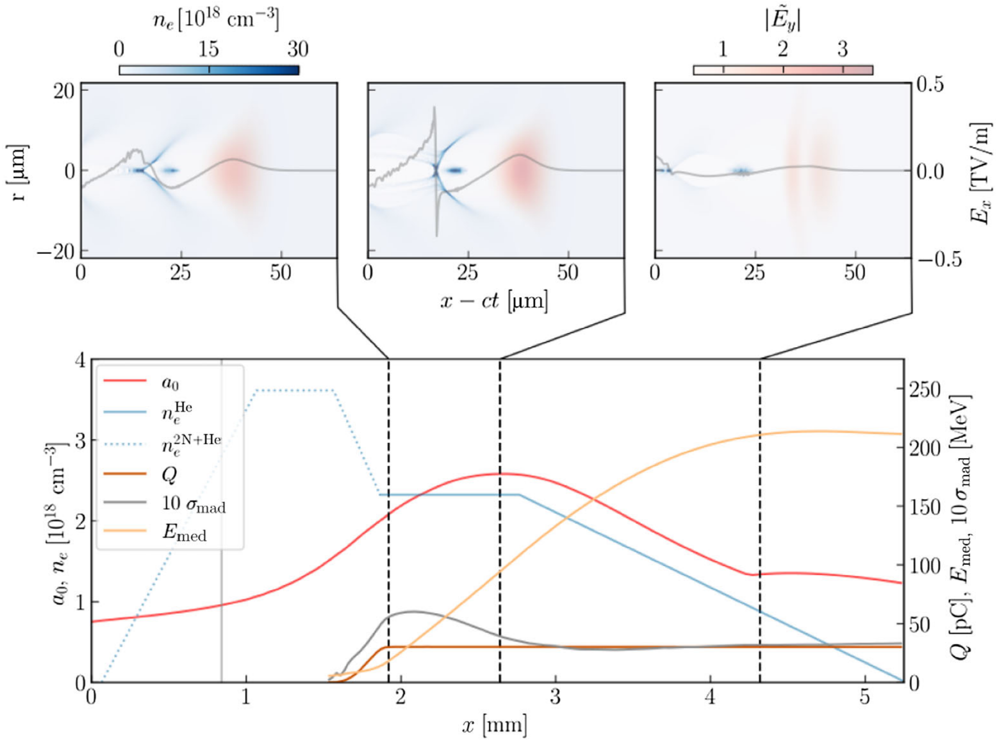

FIG. 8. Evolution of laser ($a_0$) and beam parameters ($Q$, $E_{\mathrm{med}}$, $\sigma_{\mathrm{mad}}$) during propagation for configuration 7516. The electron density profile for chamber 1 (dashed line) and chamber 2 (solid line) is added. Laser travels from left to right. Three snapshots display the injection process at three different timesteps (increase of $a_0$, maximum of $a_0$, and beam at plasma outramp). Entrance of chamber 1 is located at $x = 1$ mm.

guiding during propagation. An early injection starts in chamber 1 around $x = 1$ mm and lasts for almost 1 mm, while the injection for configuration 7516 starts very late at $x = 1.8$ mm (typically the entrance of chamber 2) and stops 0.2 mm later.

The charge $Q$ reaches its maximum at beginning of chamber 2 (zone where the dopant is no longer present) for both cases. For configuration 3702, one sees that $Q$ then decreases during propagation. This comes from the presence of a second bunch (whose charge is also accounted for in $Q$) behind the bubble which tends to slip out of the box during propagation.

Beam loading is present for both configurations and even surprisingly for the lower charge case (30 pC). It is clearly visible in Fig. 8, where the longitudinal accelerating field $E_x$ becomes almost constant along the bunch. For the higher charge case, the observed high value of $a_0$ (almost twice higher) mitigates the beam-loading effect (typical sharp bubble shape as observed in the laser-dominated regime [43]).

For configuration 7516, the propagation in chamber 2 has a positive effect on the energy spread $\sigma_{\mathrm{mad}}$, while its effect is less noticeable for configuration 3702. As a matter of fact, the longitudinal accelerating field $E_x$ is not constant along the bunch for configuration 3702 (beam loading is not optimal).

As expected, chamber 2 (including the downramp) clearly plays its role for accelerating the bunch.

The careful analysis of these two configurations shows that the cell design is particularly relevant: chamber 1 allows for self-focusing triggering injection and chamber 2 is efficiently designed for energy increase and energy spread reduction.

These two particular configurations show the clear influence of beam loading in the final energy spread. Self-focusing is the key parameter to trigger upstream injection.

## IV. CONCLUSION AND OPENING

Starting from a robust plasma target design composed of two chambers, with dopant mitigated in the first part, the random scans dataset presented here allowed for the generation of a large number of electron beams parameters satisfying the initial filter "$Q > 30$ pC & $E_{\mathrm{med}} > 150$ MeV & $\delta E_{\mathrm{mad}} < 5\%$ & $\epsilon_y < 2$ μm" with origins from different input configurations (LPI working points). This was allowed by fast simulations with the SMILEI code combined with computing time allocated by GENCI at TGCC.

Beams matching the filter corresponded to a laser focus in vacuum placed at the end of the accelerating chamber. Plasma self-focusing allowed for an earlier injection and longer accelerating distance (typically all along chamber 2).

The divergence was outside of the scope but previous works proved the efficiency of plasma outramp to deal with this issue. This work could be done as a postprocess of the present results.

All present results are left open to the scientific community so that any researcher may use them to find optimal working points for a specific LPI, even including artificial intelligence and machine learning studies.

## ACKNOWLEDGMENTS

This work was granted access to the HPC resources of TGCC under the allocations 2021—A0110510062 and 2022—A0130510062 made by GENCI for the project Virtual Laplace.

[1] O. Brüning, H. Burkhardt, and S. Myers, The Large Hadron Collider, Prog. Part. Nucl. Phys. **67**, 705 (2012).

[2] M. Benedikt, V. Mertens, F. Zimmermann, F. Cerutti, T. Otto, J. Poole, O. Brunner, J. Gutleber, A. Milanese, A. Blondel *et al.*, FCC-ee: The lepton collider: Future circular collider conceptual design report volume 2, Eur. Phys. J. Spec. Top. **228**, 261 (2018).

[3] E. Esarey and M. Pilloff, Trapping and acceleration in nonlinear plasma waves, Phys. Plasmas **2**, 1432 (1995).

[4] J. Faure, Accélération de particules par interaction laser-plasma dans le régime relativiste, Ph.D. thesis, Université Paris Sud-Paris XI, 2009.

[5] L. Labate, D. Palla, D. Panetta, F. Avella, F. Baffigi, F. Brandi, F. Di Martino, L. Fulgentini, A. Giulietti, P. Köster *et al.*, Toward an effective use of laser-driven very high energy electrons for radiotherapy: Feasibility assessment of multi-field and intensity modulation irradiation schemes, Sci. Rep. **10**, 17307 (2020).

[6] D. Oumbarek Espinos, High quality laser driven electron beams for undulator and free electron laser radiation, Ph.D. thesis, Université Paris-Saclay, Osaka University, 2021.

[7] S. Jalas, M. Kirchen, P. Messner, P. Winkler, L. Hübner, J. Dirkwinkel, M. Schnepp, R. Lehe, and A. R. Maier, Bayesian Optimization of a Laser-Plasma Accelerator, Phys. Rev. Lett. **126**, 104801 (2021).

[8] M. Kirchen, S. Jalas, P. Messner, P. Winkler, T. Eichner, L. Hübner, T. Hülsenbusch, L. Jeppe, T. Parikh, M. Schnepp *et al.*, Optimal Beam Loading in a Laser-Plasma Accelerator, Phys. Rev. Lett. **126**, 174801 (2021).

[9] A. Gonsalves, K. Nakamura, J. Daniels, C. Benedetti, C. Pieronek, T. De Raadt, S. Steinke, J. Bin, S. Bulanov, J. Van Tilborg *et al.*, Petawatt Laser Guiding and Electron Beam Acceleration to 8 GeV in a Laser-Heated Capillary Discharge Waveguide, Phys. Rev. Lett. **122**, 084801 (2019).

[10] G. Golovin, S. Chen, N. Powers, C. Liu, S. Banerjee, J. Zhang, M. Zeng, Z. Sheng, and D. Umstadter, Tunable monoenergetic electron beams from independently controllable laser-wakefield acceleration and injection, Phys. Rev. ST Accel. Beams **18**, 011301 (2015).

[11] J. P. Couperus, R. Pausch, A. Köhler, O. Zarini, J. M. Krämer, M. Garten, A. Huebl, R. Gebhardt, U. Helbig,

S. Bock *et al.*, Demonstration of a beam loaded nanocoulomb-class laser wakefield accelerator, Nat. Commun. **8**, 487 (2017).

[12] F. Albert, M. Couprie, A. Debus, M. C. Downer, J. Faure, A. Flacco, L. A. Gizzi, T. Grismayer, A. Huebl, C. Joshi *et al.*, 2020 roadmap on plasma accelerators, New J. Phys. **23**, 031101 (2021).

[13] P. Lee, G. Maynard, T. Audet, B. Cros, R. Lehe, and J.-L. Vay, Optimization of laser-plasma injector via beam loading effects using ionization-induced injection, Phys. Rev. Accel. Beams **21**, 052802 (2018).

[14] J. P. Couperus, Optimal beam loading in a nanocoulomb-class laser wakefield accelerator, Helmholtz-Zentrum Dresden-Rossendorf, Germany, Technical Report, 2018.

[15] J. Derouillat, A. Beck, F. Pérez, T. Vinci, M. Chiaramello, A. Grassi, M. Flé, G. Bouchard, I. Plotnikov, N. Aunai *et al.*, Smilei: A collaborative, open-source, multi-purpose particle-in-cell code for plasma simulation, Comput. Phys. Commun. **222**, 351 (2018).

[16] https://pallas.ijclab.in2p3.fr/.

[17] https://laserix.ijclab.in2p3.fr/en/laserix-2-2/.

[18] http://www.eupraxia-project.eu/.

[19] X. Li, A. Chancé, and P. A. P. Nghiem, Preserving emittance by matching out and matching in plasma wakefield acceleration stage, Phys. Rev. Accel. Beams **22**, 021304 (2019).

[20] A. R. Rossi, V. Petrillo, A. Bacci, E. Chiadroni, A. Cianchi, M. Ferrario, A. Giribono, M. R. Conti, L. Serafini, and C. Vaccarezza, Angstrom wavelength FEL driven by 5 GeV IWFA beam with external injection, J. Phys. Conf. Ser. **1596**, 012004 (2020).

[21] F. Gori, Flattened Gaussian beams, Opt. Commun. **107**, 335 (1994).

[22] S. Kuschel, M. Schwab, M. Yeung, D. Hollatz, A. Seidel, W. Ziegler, A. Sävert, M. Kaluza, and M. Zepf, Controlling the Self-Injection Threshold in Laser Wakefield Accelerators, Phys. Rev. Lett. **121**, 154801 (2018).

[23] A. Pak, K. Marsh, S. Martins, W. Lu, W. Mori, and C. Joshi, Injection and Trapping of Tunnel-Ionized Electrons into Laser-Produced Wakes, Phys. Rev. Lett. **104**, 025003 (2010).

[24] M. Vargas, W. Schumaker, Z.-H. He, Z. Zhao, K. Behm, V. Chvykov, B. Hou, K. Krushelnick, A. Maksimchuk, V. Yanovsky *et al.*, Improvements to laser wakefield accelerated electron beam stability, divergence, and energy spread using three-dimensional printed two-stage gas cell targets, Appl. Phys. Lett. **104**, 174103 (2014).

[25] P. Lee, G. Maynard, T. Audet, B. Cros, R. Lehe, and J.-L. Vay, Dynamics of electron injection and acceleration driven by laser wakefield in tailored density profiles, Phys. Rev. Accel. Beams **19**, 112802 (2016).

[26] T. Audet, P. Lee, G. Maynard, S. D. Dufrénoy, A. Maitrallain, M. Bougeard, P. Monot, and B. Cros, Gas cell density characterization for laser wakefield acceleration, Nucl. Instrum. Methods Phys. Res., Sect. A **909**, 383 (2018).

[27] https://www.openfoam.com/.

[28] A. Beck, J. Dérouillat, M. Lobet, A. Farjallah, F. Massimo, I. Zemzemi, F. Perez, T. Vinci, and M. Grech, Adaptive SIMD optimizations in particle-in-cell codes with fine-grain particle sorting, arXiv:1810.03949.

[29] F. Massimo, A. Beck, J. Derouillat, M. Grech, M. Lobet, F. Pérez, I. Zemzemi, and A. Specka, Efficient start-to-end 3D envelope modeling for two-stage laser wakefield acceleration experiments, Plasma Phys. Controlled Fusion **61**, 124001 (2019).

[30] C. Benedetti, C. B. Schroeder, E. Esarey, C. G. R. Geddes, and W. P. Leemans, Efficient modeling of laser-plasma accelerators with INF&RNO, AIP Conf. Proc. **1299**, 250 (2010).

[31] P. Tomassini, S. De Nicola, L. Labate, P. Londrillo, R. Fedele, D. Terzani, and L. A. Gizzi, The resonant multi-pulse ionization injection, Phys. Plasmas **24**, 103120 (2017).

[32] F. Massimo, I. Zemzemi, A. Beck, J. Dérouillat, and A. Specka, Efficient cylindrical envelope modeling for laser wakefield acceleration, Phys. Rev. E **102**, 033204 (2020).

[33] M. Santarsiero, D. Aiello, R. Borghi, and S. Vicalvi, Focusing of axially symmetric flattened Gaussian beams, J. Mod. Opt. **44**, 633 (1997).

[34] FBPIC laser profiles (2022), https://fbpic.github.io/api_reference/lpa_utilities/laser_profiles/flattened.html.

[35] E. Esarey, C. B. Schroeder, and W. P. Leemans, Physics of laser-driven plasma-based electron accelerators, Rev. Mod. Phys. **81**, 1229 (2009).

[36] GENCI center for high-performance computing and processing data (2022), https://www.genci.fr/en.

[37] https://en.wikipedia.org/wiki/Skew_normal_distribution.

[38] https://gitlab.in2p3.fr/lpa-pic-simulations-data/randomscans.

[39] https://github.com/SmileiPIC/Smilei/tree/master/happi.

[40] W. Lu, M. Tzoufras, C. Joshi, F. Tsung, W. Mori, J. Vieira, R. Fonseca, and L. Silva, Generating multi-GeV electron bunches using single stage laser wakefield acceleration in a 3D nonlinear regime, Phys. Rev. ST Accel. Beams **10**, 061301 (2007).

[41] I. Dornmair, K. Floettmann, and A. Maier, Dedicated matching sections for divergence reduction in a laser plasma acceleration stage, AIP Conf. Proc. **1777**, 040011 (2016).

[42] L. Dickson, C. Underwood, F. Filippi, R. Shalloo, J. B. Svensson, D. Guénot, K. Svendsen, I. Moulanier, S. D. Dufrénoy, C. Murphy *et al.*, Mechanisms to control laser-plasma coupling in laser wakefield electron acceleration, Phys. Rev. Accel. Beams **25**, 101301 (2022).

[43] J. Götzfried, A. Döpp, M. Gilljohann, F. Foerster, H. Ding, S. Schindler, G. Schilling, A. Buck, L. Veisz, and S. Karsch, Physics of High-Charge Electron Beams in Laser-Plasma Wakefields, Phys. Rev. X **10**, 041015 (2020).